Imaging plasma membrane domains in signal transduction pathways

Pezzarossa, A.

Chapter 4

Microseconds single-molecule tracking[1]

Here we report on a method to track individual molecules on nanometer length and microsecond time scales using an optical microscope. Our method is based on double-labeling of a molecule with two spectrally distinct fluorophores and illuminating it with laser pulses of different wavelengths that partially overlap temporally. We demonstrate our method by using it to resolve the motion of short DNA oligomers diffusing in solution down to a time scale of 100 μs.

[1]This chapter is based on: Semrau, S., Pezzarossa, A., Schmidt, T. (2011) Microseconds single molecule tracking (μsSMT). *Biophys. J.* **100**, L19-21.

4.1 Introduction

A persistent challenge in biophysics is resolving the motion of single biomolecules in short length and fast time scales (1). The relevant length scale is typically on the order of tens of nanometers and the time scale is on the order of tens of microseconds. Recent advances in superresolution techniques (2–5) are beginning to give us the first images of biomolecules with nanometer resolution. However, these techniques are severely limited in their temporal resolution as they either require scanning the sample, such as STED (STimulated Emission Depletion) microscopy, or acquiring the acquisition of stochastically occurring signals, as in STORM (STOchastic Reconstruction Microscopy) and PALM (Photo-Activation Localization Microscopy) (2). These techniques cannot access the fast dynamic interaction of mobile biomolecules with nanometer sized structures. For example, the interaction of a lipid molecule diffusing in a cell membrane (diffusion coefficient $D \approx 1\ \mu\mathrm{m}^2/\mathrm{s}$) with a membrane substructure that has a characteristic length L of about 50 nm occurs on a time scale $t \approx L/4D \approx 1$ ms. Consequently, observing the interaction of molecules with nanometer sized structures requires techniques with sub-ms temporal resolution. Here we present a new camera-based, thus highly parallel, Single-Molecule Tracking (SMT) method that fulfills this requirement.

The two major factors which determine the temporal resolution of camera-based SMT (6) are the acquisition speed of the CCD camera and the illumination time necessary to detect the optical probe. During the illumination time the probe must emit enough photons to be detected above the read-out noise of the camera. At the same time, the read-out noise generally increases with the read-out speed of the camera. Consequently, SMT on microsecond time scales could so far only be realized with colloidal gold probes (7). Although such colloidal probes are bright and optically stable, they are not optimal for biological applications because of their large size and unspecific binding issues. In contrast, our method uses small fluorophores in combination with a slow-scan, low readout-noise CCD camera system to achieve microsecond Single-Molecule Tracking (μsSMT). μsSMT is comparable to STORM in that it uses two fluorescent probes on a single molecule. In contrast to STORM, these probes are placed so far apart that no energy transfer can take place between them and thus the two are excited separately.

4.2 Material and Methods

4.2.1 DNA Construct

The molecule tracked in the experiments described here was a fluorescently labeled 155 basepair (bp) DNA construct containing a 601 nucleosome positioning sequence (9). The DNA was prepared by PCR and was labeled with biotin, Cy3B and ATTO647N by incorporation of fluorescently labeled, HPLC purified primers (IBA GmbH). PCR primers were as follows: 5'-TTGG CTGGAGAATC CCGGTGCCGA GGCCGCTCAA TTGGTCGTAG ACAGCTCTAG CACCGCTTAA ACGCACGTAC GCGCTG-3' (Cy3B-labeled nucleotide is underlined) 5'-biotin-TTGGACAGGA TGTATATATC TGACACGTGC CTGGAGACTA GGGAGTAATC CCCTTGGCGG TTAAAACGCG GGGGACAGC-3' (ATTO647N-labeled nucleotide is underlined) In the DNA the Cy3B and the ATTO647N were located 76 bp (24 nm) apart. Since this distance was significantly bigger than the Förster radius of the fluorophores ($\approx$ 5.5 nm) there was no FRET as confirmed by FCS experiments (data not shown).

4.2.2 Single-molecule microscopy

The experimental setup for single-molecule imaging has been described in detail previously (2). Briefly, the microscope (Axiovert 100; Zeiss) was equipped with a 100$\times$ oil-immersion objective (NA=1.4, Zeiss, Oberkochen, Germany). The samples were illuminated for $t_{\mathrm{ill}} = 1$ ms, 3 ms or 5 ms by an Ar^+ laser (Spectra Physics) with a wavelength of 514 nm and a 30 mW diode laser (Power technology) with a wavelength of 639 nm. The length of the laser pulses t_{ill} and the time lag between the pulses Δt were set by an acousto-optical tunable filter (AOTF) (AA Electrooptique). The illumination intensity was set to $3 \pm 0.3\,\mathrm{kW/cm^2}$ for both lasers. A circular diaphragm was introduced in the back focal plane of the tube lens to confine the illumination area and create a flat laser illumination profile. An appropriate filter combination (dichroic Z405/514/647/1064rpc and emission filter Z515/647m, Chroma Technology) permitted the detection of individual fluorophores by a liquid nitrogen cooled slow-scan CCD camera system (Princeton Instruments). A dichroic wedge diverted the emitted light to two different regions of the CCD according to emission wavelength, see figure 4.1. In this way the fluorescence signals from the Cy3B and ATTO647N molecules were separated. For the observation of the diffusion

of single DNA molecules in solution, the molecules were dissolved in phosphate buffered saline (PBS: 150mM NaCl, 10 mMNa_2HPO_4/NaH_2PO_4, pH 7.4), 5% dextran T500 / PBS or 10% dextran T500 / PBS. 1 of the solution was placed on a cover slip in a custom made sample holder and the focus of the microscope was set several μm into the solution (depth of focus ≈ 1 μm). The number of molecules in the focal volume was chosen so low that individual fluorophores could be resolved.

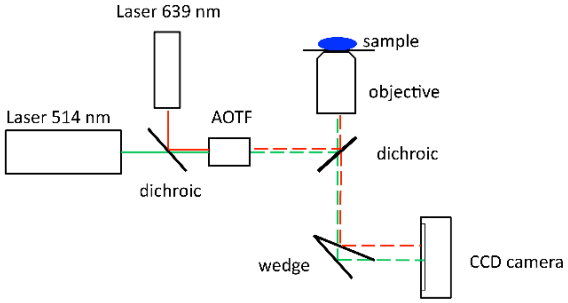

Figure 4.1: Microscope setup. Two lasers (514 nm and 639 nm) were focused on the backfocal plane of a high NA objective which resulted in widefield illumination of the sample. The fluorescence light from the red and green fluorophores respectively was split by a dichroic wedge and directed to different regions on the CCD chip. The two lasers were pulsed independently by an AOTF.

4.2.3 Fitting of single-molecule signals

Details about finding and fitting single-molecule signals were described elsewhere (1, 6). Briefly, raw images were filtered with a two-dimensional Gaussian whose width corresponds to the width of the point spread function (PSF) of the microscope. This procedure optimized the signal to noise ratio. The positions of the pixels whose value after filtering exceeded a certain multiple of the noise were used as initial values for the fitting of a two-dimensional Gaussian in the unfiltered image. This thresholding procedure separated true single-molecule signals from noise. From the Gaussian fit, position, width and integrated intensity of the single molecule signal were determined.

4.2.4 Correction for chromatic aberration

To achieve an exact spatial correlation between the two detection channels we imaged a fluorescent bead which could be detected in both channels. The bead was adsorbed to a coverslip and moved through the whole region of interest. The positions of the bead in the Cy3B channel $\mathbf{s}_i^{\text{green}}$ and the the ATTO647N channel $\mathbf{s}_i^{\text{red}}$ were determined as described in the previous section. To interpolate the shift for areas which had not been covered by the bead fifth-order polynomials $f_x(\mathbf{s})$ and $f_y(\mathbf{s})$ were fit to the measured positions (separately for the two directions x and y) so that

$$\sum_i (f_x(\mathbf{s}_i^{\text{green}}) - (x_i^{\text{red}} - x_i^{\text{green}}))^2 = \text{minimal !}$$
$$\sum_i (f_y(\mathbf{s}_i^{\text{green}}) - (y_i^{\text{red}} - y_i^{\text{green}}))^2 = \text{minimal !}$$

$f_x(\mathbf{s})$ and $f_y(\mathbf{s})$ then gave the corrective shifts – in x and y respectively– to be applied to a position measured in the green channel. figure 1d in section 4.3 shows an example for these shifts.

4.2.5 Particle image cross-correlation spectroscopy

Particle image cross-correlation spectroscopy (PICCS) calculates the correlation function between two 2 different types of signals termed "green" and "red" without loss of generality. The PICCS algorithm illustrated in figure 4.2 results in the cumulative correlation function $C_{\text{cum}}(r^2, \Delta t)$ where Δt is the time-lag between the illumination of the two probes.

If, per image, there is exactly one pair of correlated signals the correlation function $C_{\text{cum}}\,(r^2, \Delta t)$ equals $P_{\text{cum}}\,(r^2, \Delta t)$, the probability for finding a distance smaller than r between a green and a red signal. If only for a fraction β_{g} of all green signals there is a correlated red signal, we observe $C_{\text{cum}}\,(r^2, \Delta t) = \beta_{\text{g}} P_{\text{cum}}\,(r^2, \Delta t)$. Typically there is more than one green signal per image and therefore also more than one red signal. If r gets bigger, neighboring red signals in close proximity are counted by the PICCS algorithm although they are not correlated with the green signal. Additionally there might be red signals which are not correlated with any green signal at all. These red signals, in close proximity or not correlated with any green signal, lead to an additional contribution $c_{\text{red}}\pi r^2$ to $C_{\text{cum}}(r^2, \Delta t)$. Here we assume that the positions of the red signals follow a uniform random distribution with density c_{red}. In total

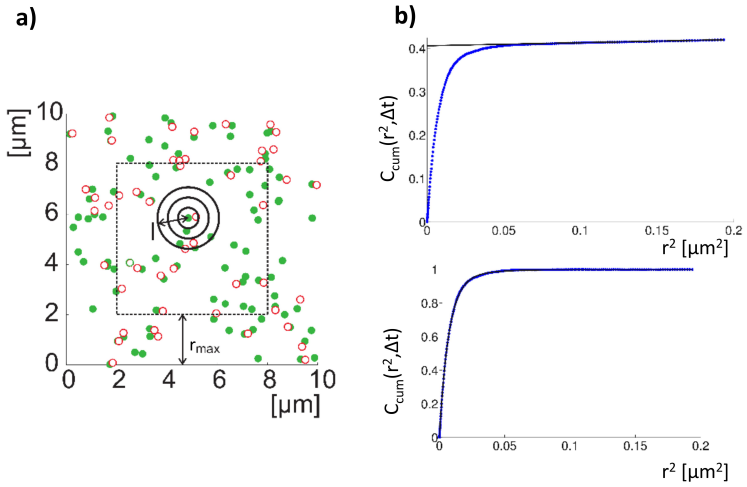

Figure 4.2: a) PICCS algorithm. For all green signals (solid circles) the number of red signals (open circles) are counted which fall into a circle of radius r from a green signal. The total number is divided by the number of green signals. By increasing r from 0 to $r_{\max}$ the whole correlation function $C_{\mathrm{cum}}(r^2, \Delta t)$ is constructed. To avoid edge effects, only the green signals in the area bounded by the dashed line are used. Those signals lie farther away from the edges of the image than the maximal distance $r_{\max}$ analyzed Here $r_{\max} = 2$ μm. The signal positions were simulated with these parameters: density of green signals $c_{\mathrm{green}} = 1$ $\mu\mathrm{m}^{-2}$, correlation fraction $\beta_{\mathrm{g}} = 0.5$ (results in a density of red signals of $c_{\mathrm{red}} = 0.5$ $\mu\mathrm{m}^{-2}$), correlation length $\sigma = 150$ nm.**b)** Examples for top $C_{\mathrm{cum}}(r^2, \Delta t)$ and bottom $P_{\mathrm{cum}}(r^2, \Delta t)$ found in experiments with $\Delta t = 0.3$ ms, $t_{\mathrm{ill}} = 3$ ms. The solid black line in the top graph is a linear fit to the linear part of $C_{\mathrm{cum}}(r^2, \Delta t)$ plotted against r^2. This linear contribution is subtracted and the resulting curve is normalized to one to obtain $P_{\mathrm{cum}}(r^2, \Delta t)$ shown in the bottom graph. The solid black line in the bottom graph is a fit of Eq. 4.2 to the data.

$C_{\mathrm{cum}}(r^2, \Delta t) = \beta_{\mathrm{g}} P_{\mathrm{cum}}(r^2, \Delta t) + c_{\mathrm{red}} \pi r^2$.

If there are no red signals in addition to the ones correlated with a green one, c_{red} can be calculated from the density of green signals c_{green}, the correlation fraction β_{g} and the image area A by:

$$c_{\mathrm{red}} = \beta_{\mathrm{g}}(c_{\mathrm{green}} A - 1)/A = \beta_{\mathrm{g}}(c_{\mathrm{green}} - 1/A) \equiv c^*_{\mathrm{red}} \qquad (4.1)$$

If $1/A \ll c_{\mathrm{green}}$, $c_{\mathrm{red}} \approx \beta_{\mathrm{g}} c_{\mathrm{green}}$. In general $c_{\mathrm{red}} = c^*_{\mathrm{green}} + c_{\mathrm{red,\ uncorr.}}$, where $c_{\mathrm{red,\ uncorr.}}$ is the density of red signals which are nor correlated with any green signal.

In practice $P_{\mathrm{cum}}(r^2, \Delta t)$ is retrieved by subtraction of the linear part of $C_{\mathrm{cum}}(r^2, \Delta t)$ when plotted against r^2 and subsequent normalization to 1, see figure 4.2 b.

Since the probability to find exactly the distance r between a green and a red signal is $\partial P_{\mathrm{cum}}(r^2, \Delta t)/\partial r$ the MSD could in principle be calculated by $\overline{MSD}(\Delta t) = \int_0^\infty dr\, r^2 \partial P_{\mathrm{cum}}(r^2, \Delta t)/\partial r$. Due to noise this direct calculation would lead to large errors. Instead the heuristic formula

$$P_{\mathrm{cum}}(r^2, \Delta t) = 1 - \left[\alpha \exp\left(-\frac{r^2}{4D_1 \Delta t}\right) + (1-\alpha)\exp\left(-\frac{r^2}{4D_2 \Delta t}\right)\right], \tag{4.2}$$

was fit to $P_{\mathrm{cum}}(r^2, \Delta t)$ with 3 fit parameters α, D_1 and D_2, which gave a good description of the data in all cases and eliminated high-frequency noise, see figure 4.2b. The MSD is then simply $\overline{MSD}(\Delta t) = \alpha 4 D_1 \Delta t + (1-\alpha) 4 D_2 \Delta t$.

Finally we have to take into consideration that the positions of single-molecules can be determined only with a finite positional accuracy. The probability $P(\xi, \eta, \Delta t)$ to observe two correlated signals separated by a vector (ξ, η) is the convolution of the real probability $P_{\mathrm{real}}(\xi, \eta, \Delta t)$ and the probability density $P_{\text{pos. acc.}}(\xi, \eta)$ describing the (apparent) correlation due to the finite positional accuracy (10).

$$\begin{aligned} P(\xi, \eta, \Delta t) &= \int\int d\xi'\, d\eta' P_{\mathrm{real}}(\xi - \xi', \eta - \eta', \Delta t) P_{\text{pos. acc.}}(\xi', \eta') \\ P_{\text{pos. acc.}}(\xi, \eta) &= \frac{1}{2\pi\sigma^2} \exp\left(-\frac{\xi^2 + \eta^2}{2\sigma^2}\right) \end{aligned} \tag{4.3}$$

where $\sigma = \sqrt{2}\sigma_{\text{pos. acc.}}$ and $\sigma_{\text{pos. acc.}}$ is the one-dimensional positional accuracy. For simplicity we assume here that the positional accuracy is the same for both types of signals. The cumulative probability $P_{\mathrm{cum}}\ (r^2, \Delta t)$ is then found by integration of $P(\xi, \eta, \Delta t)$ in polar coordinates

$$P_{\mathrm{cum}}\ (r^2, \Delta t) = \int_0^{2\pi} d\phi \int_0^r dr P(r, \phi, \Delta t) \tag{4.4}$$

with $r = \sqrt{\xi^2 + \eta^2}$, $\phi = \arctan(\eta/\xi)$.

The MSD calculated from this cumulative probability has a constant contribution $4\sigma^2$ as already mentioned above.

4.2.6 Error determination

The error bars in figure 4.4 in the results section were determined from Monte Carlo simulations of the probability $P_{\text{cum}}(r^2, \Delta t)$ with exactly the same parameters as found in the experiments and the number of molecule positions actually recorded. For each simulation the MSD was determined as described in the previous section and the standard deviation calculated from 100 simulations run with identical parameters.

4.2.7 FCS measurements

FCS measurements were performed on a home-made confocal microscope described in detail elsewhere (9). The measured auto-correlation curves $G(t)$ were fit to a model for 3D diffusion.

$$G(t) = \frac{G_0}{(1 + t/\tau_d)\sqrt{(1 + (a^{-2})(t/\tau_d))}}$$

with the free parameters G_0, the auto-correlation amplitude, a, a geometric factor equal to the ratio of width and height of the focal volume, and τ_d, the diffusion time. Errors were determined as errors of the fit of the model to the measured curves.

4.2.8 Viscosity measurements

Bulk kinematic viscosity measurements were performed with a Cannon-Ubbelohde viscometer (CANNON Instrument Company,State College, PA, USA). Measurements of all different solvents used were conducted in triplicates and the error determined as the standard deviation.

4.3 Results

In our experiments the emitted signal of the two fluorophores is collected onto separate regions of a CCD chip with the help of a dichroic wedge as shown in Figure 4.1 a. In this way the two fluorophores are separately excited and their fluorescent signals recorded independently of each other. Therefore, we can resolve the position of a single molecule with a nanometer resolution at two different points in time. In principle, we can make the interval between the two time points arbitrarily small. The actual temporal resolution achievable in practice is primarily determined by the

molecule's diffusion coefficient, the accuracy with which we can determine the molecular positions, and the total number of single-molecule positions measured.

To demonstrate our method, we used short DNA-oligonucleotides that were labeled with two fluorophores, Cy3B and ATTO647N. These probes were then separately illuminated by two lasers at wavelengths of 514 nm and 639 nm, respectively, during time periods of length t_{ill} (illumination time). The pulses of the two lasers were temporally offset by a small time lag Δt (see figure 4.3a). In principle, we can make Δt arbitrarily small.

Since the illumination time was finite, we did not measure the actual positions $\mathbf{s}(t)$ and $\mathbf{s}(t+\Delta t)$. Instead, our method measures the positions $\overline{\mathbf{s}(t)}$ and $\overline{\mathbf{s}(t+\Delta t)}$ averaged over the illumination period t_{ill}. Due to this temporal averaging the mean squared-displacement (MSD) calculated from measured positions was different from the actual MSD of the molecule(14). For ergodic and stationary processes there is, however, a simple relation between the observed (averaged) $\overline{\mathrm{MSD}}(\Delta t)$ and the actual MSD of the molecule

$$\begin{aligned}\overline{\mathrm{MSD}}(\Delta t) &= \left\langle \left(\overline{\mathbf{s}(t+\Delta t)} - \overline{\mathbf{s}(t)}\right)^2 \right\rangle \\ &= \frac{1}{t_{\mathrm{ill}}^2}\int_{-t_{\mathrm{ill}}}^{0} dt' \int_{-t_{\mathrm{ill}}-t'}^{-t'} d\varepsilon \left(\mathrm{MSD}(\Delta t+\varepsilon) - \mathrm{MSD}(\varepsilon)\right) \end{aligned} \tag{4.5}$$

Since the microscope projects the three dimensional movement of the molecules in solution onto a two dimensional plane, $\mathrm{MSD}(\Delta t) = 4D\Delta t$. For regular diffusion Eq. 4.5 was evaluated analytically (see **Appendix 4.A** for the derivation of the general relation and the analytical evaluation).

$$\overline{\mathrm{MSD}}(\Delta t) = 4D \times \begin{cases} \left(\frac{\Delta t^2}{t_{\mathrm{ill}}} - \frac{1}{3}\frac{\Delta t^3}{t_{\mathrm{ill}}^2}\right) & \text{for} \quad \Delta t \le t_{\mathrm{ill}} \\ \left(\Delta t - \frac{1}{3}t_{\mathrm{ill}}\right) & \text{for} \quad \Delta t \ge t_{\mathrm{ill}} \end{cases} \tag{4.6}$$

Below we will show that the measured $\overline{\mathrm{MSD}}(\Delta t)$ indeed behaved as predicted by eq. 4.6.

The calculation of a molecule's MSD requires the determination of its position. In our experiments we chose a low density of molecules such that molecules were resolved individually and their position determined

with nanometer positional accuracy (6). figure 4.3 illustrates the process of position determination. figure 4.3b and figure 4.3c show typical raw signals from several molecules dual-labeled with Cy3B (figure 4.3b) and ATTO647N (figure 4.3c). The positions of the fluorophores were determined by fitting two-dimensional Gaussians approximating the point spread function of the microscope. The positional accuracy achieved was between 40 nm and 50 nm (see section 4.2). Since the signals from the two fluorophores labeling the single molecule had to be correlated, eliminating chromatic aberration was important. We established the correspondence between the two signals by using fluorescent beads which were observable in both channels. figure 4.3d shows the corrective shifts which were applied to the signals in the green (or red) channel, respectively. Figure 4.3e shows the single-molecule positions determined from figure 4.3b and c and corrected for chromatic aberration. Note that due to the finite fluorophore binding efficiency some molecules carried no or only one of the labels.

To determine the MSD of the molecules, we correlated the positions that were measured in the two detection channels by particle image cross-correlation spectroscopy (PICCS), that we have developed as an extension of PICS (Particle Image Correlation Spectroscopy) (15). Figure 4.4 shows a comparison of MSDs obtained experimentally under different solvent and illumination conditions. Eq. 4.6 fits the experimental data in all cases. The inset table in figure 4.4 compares the diffusion coefficients determined from the fit. As predicted, the diffusion coefficient decreased with increasing amount of dextran T500 corresponding to an increased viscosity.

Compared to the situation without the dextran the diffusion coefficient decreased by a factor of 3.4 ± 0.9 in the solution with 5% dextran T500 and by a factor of 5.8 ± 1.0 in the solution with 10 % dextran T500, see inset table in figure 4.4b. We confirmed our results by independent FCS (Fluorescence Correlation Spectroscopy) measurements (data not shown) of the same DNA construct in the same solvents in which we found factors of 3.20 ± 0.04 and 6.05 ± 0.06 between the corresponding diffusion times, respectively. Interestingly the diffusion coefficient did not scale with the bulk kinematic viscosity, which increased by a factor of 6.2 ± 0.1 in the solution with 5% dextran T500 and by a factor of 20.9 ± 0.2 in the solution with 10% dextran T500, as determined by bulk viscosity measurements. This deviation probably reflects the fact that solvent and solute molecules were comparable in size for which the Stokes-Einstein relation is invalid.

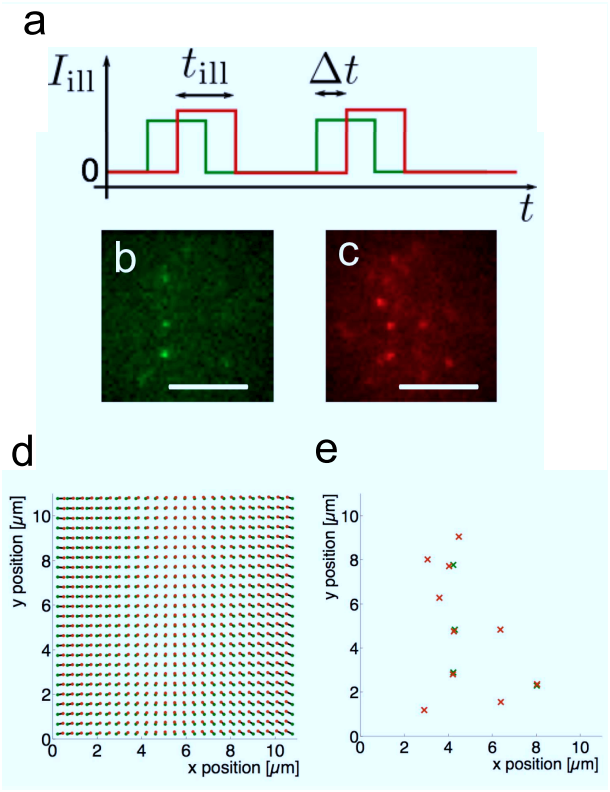

Figure 4.3: Illumination scheme and position determination. **a)** Laser pulses of duration t_{ill} are temporally offset by a time lag Δt **b)** Raw image from the Cy3B channel (c) Raw image from the ATTO647N channel. Both images were taken at the same time ($\Delta t = 0$), scale bar: 5 μm. **d)** Correction for chromatic aberration. The scheme shows positions in the Cy3B (green dots) and ATTO647N (red dots) channel which correspond to the same physical positions. **e)** Identified single-molecule signals from the images shown in (b) and (c) corrected for chromatic aberration.

For non-overlapping laser pulses ($\Delta t > t_{\mathrm{ill}}$) the observed MSD was shifted down by $(4/3)Dt_{\mathrm{ill}}$ (see figure 4.4a), in agreement with earlier results (14). For overlapping laser pulses ($\Delta t \leq t_{\mathrm{ill}}$) the MSD was clearly non-linear and approached 0 for $\Delta t \to 0$. The temporal dependence followed the prediction given by Eq. 4.6, see figure 4.4b. Most importantly, as shown in figure 4.4c, we were able to measure MSD curves down to $\Delta t = 100$ μs, significantly faster than reported so-far, which proved

that we extended single-molecule tracking experiments to the microsecond regime.

4.4 Conclusions

Our method may be further improved by eliminating the need for double labeling. Given that the fluorescent probe is bright enough the emitted light could be split between two cameras that can be individually exposed. If the exposure of the two cameras is offset by a lag time Δt the same kind of analysis as described here can be performed with only a single fluorescent label.

Finally, μsSMT can be easily adapted for measurements in cells. For example, a membrane receptor could be labeled with two genetically encoded tags, one at a cytosolic domain and one extracellular. The separation of the two labels by the cell membrane would prevent energy transfer between the fluorophores. Since only low laser intensities are required the method is suitable for live cell recordings. Our method will likely aid in providing new insights into the dynamic behavior of molecules in cells on very short length and time scales.

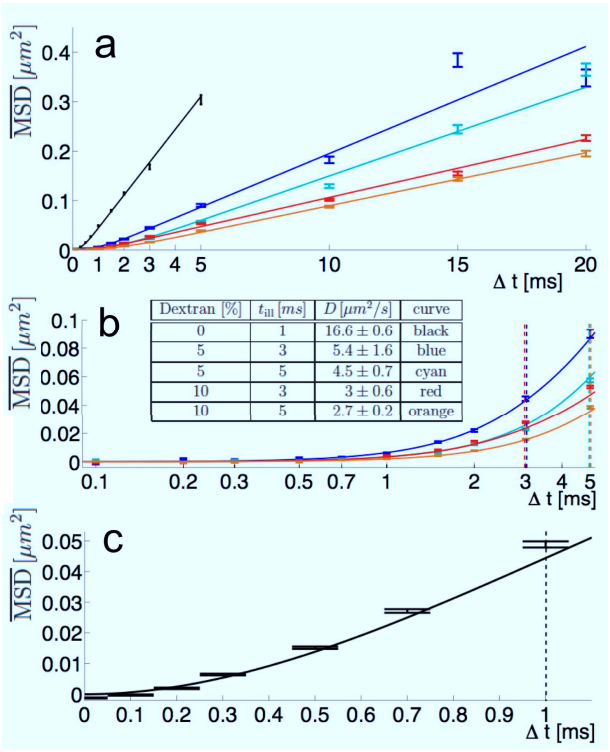

Figure 4.4: Experimentally obtained MSDs of DNA with different solvent and illumination conditions. In phosphate buffered saline (PBS), $t_{\mathrm{ill}} = 1ms$ (black), in 5% dextran T500/PBS, $t_{\mathrm{ill}} = 3ms$ (blue), in 5% dextran T500/PBS, $t_{ill} = 5ms$ (cyan), in 10% dextran T500/PBS, $t_{\mathrm{ill}} = 3ms$ (red), in 10% dextran T500/PBS, $t_{\mathrm{ill}} = 3ms$ (orange). Eq. 4.6 was fit to the data for each experimental condition (solid lines). The vertical dashed lines indicate the illumination time for the respective experiment. The error bars are standard deviations of Monte Carlo simulations performed with the measured parameters. (a) Comparison of all conditions, linear time scale. Above t_{ill} all MSDs are linear. (b) Comparison of the measurements in dextran T500 at short time lags Δt, logarithmic time scale. Below t_{ill} the MSDs show the predicted asymptotic behavior. Inset: Measured diffusion coefficients for all conditions. The reported errors are the errors of the fit to Eq. 4.6. (c) MSD on short time lags for the measurement in PBS. The MSD has data points below $t_{ill} = 1ms$ which are significantly different from 0 μm^2.

4.A Appendix

4.A.1 Derivation of theoretical result for the averaged MSD

We assume the stochastic process underlying the random walk is ergodic, which means that the ensemble average $< \ldots >$ is identical to the time average, which is the experimentally accessible quantity.

$$
\begin{aligned}
&\overline{\mathrm{MSD}}(\Delta t) \\
&= \left\langle \left(\overline{\mathbf{s}(t+\Delta t)} - \overline{\mathbf{s}(t)} \right)^2 \right\rangle \\
&= \left\langle \left(\frac{1}{t_{\mathrm{ill}}} \int_{-t_{\mathrm{ill}}}^{0} d\tilde{t}\, \mathbf{s}\left(t+\Delta t+\tilde{t}\right) - \frac{1}{t_{\mathrm{ill}}} \int_{-t_{\mathrm{ill}}}^{0} dt'\, \mathbf{s}\left(t+t'\right) \right) \right\rangle \\
&= \frac{1}{t_{\mathrm{ill}}^2} \int_{-t_{\mathrm{ill}}}^{0} d\tilde{t} \int_{-t_{\mathrm{ill}}}^{0} dt' \left\langle \left(\mathbf{s}(t+\Delta t+\tilde{t}) - \mathbf{s}(t+t')\right)^2 - \mathbf{s}^2(t+\Delta t+\tilde{t}) - \mathbf{s}^2(t+t') \right. \\
&\qquad \left. \left(+\mathbf{s}(t+t')\mathbf{s}(t+\tilde{t}) + \mathbf{s}(t+\Delta t+\tilde{t})\mathbf{s}(t+\Delta t+t')\right) \right\rangle
\end{aligned}
\tag{4.7}
$$

In the last step we expanded the brackets, regrouped the terms and switched the time integral with taking the ensemble average, which is admissible because taking the ensemble average is a linear operation. We further assume that the stochastic process is second-order stationary, i.e.

$$
\left\langle \mathbf{s}(\tau)\mathbf{s}(\tau') \right\rangle = \left\langle \mathbf{s}(\tau+a)\mathbf{s}(\tau'+a) \right\rangle \tag{4.8}
$$

so that

$$
\begin{aligned}
&\overline{\mathrm{MSD}}(\Delta t) \qquad\qquad (4.9)\\
&= \frac{1}{t_{\mathrm{ill}}^2} \int_{-t_{\mathrm{ill}}}^{0} d\tilde{t} \int_{-t_{\mathrm{ill}}}^{0} dt' \left\langle \left(\mathbf{s}(\Delta t+\tilde{t}) - \mathbf{s}(t')\right)^2 \right\rangle - \left\langle \left(\mathbf{s}(\tilde{t}) - \mathbf{s}(t')\right)^2 \right\rangle \mathbf{r} \\
&= \frac{1}{t_{\mathrm{ill}}^2} \int_{-t_{\mathrm{ill}}}^{0} d\tilde{t} \int_{-t_{\mathrm{ill}}}^{0} dt' \left\langle \left(\mathbf{s}(\Delta t+\varepsilon) - \mathbf{s}(0)\right)^2 \right\rangle - \left\langle \left(\mathbf{s}(\varepsilon) - \mathbf{s}(0)\right)^2 \right\rangle \\
&\quad \text{with} \quad \varepsilon := \tilde{t} - t' \quad , \quad d\varepsilon = d\tilde{t}\mathbf{s} \\
&= \frac{1}{t_{\mathrm{ill}}^2} \int_{-t_{\mathrm{ill}}}^{0} dt' \int_{-t_{\mathrm{ill}}-t'}^{-t'} d\varepsilon \; \left(\mathrm{MSD}(\Delta t+\varepsilon) - \mathrm{MSD}(\varepsilon)\right)
\end{aligned}
\tag{4.10}
$$

For normal, two-dimensional diffusion $\mathrm{MSD}(\tau) = 4D\,|\tau|$.

$$\overline{\mathrm{MSD}}(\Delta t) = \frac{4D}{t_{\mathrm{ill}}^2} \int_{-t_{\mathrm{ill}}}^{0} dt' \int_{-t_{\mathrm{ill}}-t'}^{-t'} d\varepsilon \; |\Delta t + \varepsilon| - |\varepsilon| \tag{4.11}$$

$$I_1 := \int_{-t_{\mathrm{ill}}}^{0} dt' \int_{-t_{\mathrm{ill}}-t'}^{-t'} d\varepsilon \; |\varepsilon| = \int_{-t_{\mathrm{ill}}}^{0} dt' \, \frac{1}{2}\left[(t_{\mathrm{ill}} + t')^2 + (t')^2\right] = \frac{1}{3} t_{\mathrm{ill}}^3 \tag{4.12}$$

$$I_2 := \int_{-t_{\mathrm{ill}}}^{0} dt' \int_{-t_{\mathrm{ill}}-t'}^{-t'} d\varepsilon \; |\Delta t + \varepsilon| \tag{4.13}$$

For $\Delta t > t_{\mathrm{ill}}$ $\Delta t + \varepsilon > 0$ since $-t_{\mathrm{ill}} \le \varepsilon \le t_{\mathrm{ill}}$, so

$$I_2 = \Delta t \, t_{\mathrm{ill}}^2 + \int_{-t_{\mathrm{ill}}}^{0} dt' \int_{-t_{\mathrm{ill}}-t'}^{-t'} d\varepsilon \; \varepsilon = \Delta t \, t_{\mathrm{ill}}^2 \tag{4.14}$$

For $\Delta t \le t_{\mathrm{ill}}$

$$\begin{aligned} I_2 &= \int_{-t_{\mathrm{ill}}}^{0} dt' \int_{-t_{\mathrm{ill}}-t'+\Delta t}^{-t'+\Delta t} dz \; |z| \quad \text{with} \quad z := \Delta t + \varepsilon \quad , \quad dz = d\varepsilon \\ &= \int_{-t_{\mathrm{ill}}}^{\Delta t - t_{\mathrm{ill}}} dt' \int_{-t_{\mathrm{ill}}-t'+\Delta t}^{-t'+\Delta t} dz \; z + \int_{\Delta t - t_{\mathrm{ill}}}^{0} dt' \left(\int_{-t_{\mathrm{ill}}-t'+\Delta t}^{0} dz \; (-z) + \int_{0}^{-t'+\Delta t} dz \; z \right) \\ &= -\frac{1}{3}\Delta t^3 + \Delta t^2 \, t_{\mathrm{ill}} + \frac{1}{3} t_{\mathrm{ill}}^3 \end{aligned} \tag{4.15}$$

Combining these terms we arrive at

$$\overline{\mathrm{MSD}}(\Delta t) = \frac{4D}{t_{\mathrm{ill}}^2}\,(I_2 - I_1) = 4D \times \begin{cases} \left(\frac{\Delta t^2}{t_{\mathrm{ill}}} - \frac{1}{3}\frac{\Delta t^3}{t_{\mathrm{ill}}^2}\right) & \text{for} \quad \Delta t \le t_{\mathrm{ill}} \\ \left(\Delta t - \frac{1}{3} t_{\mathrm{ill}}\right) & \text{for} \quad \Delta t > t_{\mathrm{ill}} \end{cases} \tag{4.16}$$

Due to the finite positional accuracy there is an additional constant term which equals $2(\sigma_{\mathrm{Cy3B}}^2 + \sigma_{\mathrm{ATTO647N}}^2) =: 4\sigma^2$, where σ_{Cy3B} and $\sigma_{\mathrm{ATTO647N}}$ are the one-dimensional positional accuracies for Cy3B and ATTO647N respectively. The theoretical expression derived above plus the constant offset $4\sigma^2$ was fit to the experimentally obtained MSD with free fit parameters D and σ. The fit was a weighted least-squares fit with the inverse

square root of the errors of every data point as weights. On average $\sigma = 46$ nm. For the purpose of better comparability the offsets $4\sigma^2$ was subtracted in figure 4.4.

Bibliography

[1] Semrau, S., Schmidt, T. (2009) Membrane heterogeneity - from lipid domains to curvature effects. *Soft Matter* **5(17)** 3174-3186.

[2] Hell, S. W. (2009) Microscopy and its focal switch. *Nat. Methods* **6(1)** 24-32.

[3] Rust, M.J., Bates, M., Zhuang. X. (2006) Sub-diffraction limit imaging by stochastic optical reconstruction microscopy. (storm). *Nat. Methods* **3(10)** 793-795.

[4] Betzig, E., ... Hess, H.(2006) Imaging intracellular fluorescent proteins at nanometer resolution. *Science* **313(5793)**1642.

[5] Hess, S.T., Girirajan, T.P.K., Mason, M.D. (2006) Ultra-high resolution imaging by fluorescence photo-activation localization microscopy. *Biophys. J.* **91(11)**, 4258-4272.

[6] Schmidt,T., Schütz, G.J., Baumgartner, W., Gruber, H.J., Schindler, H. (1996) Imaging of single molecule diffusion. *Proc. Natl. Acad. Sci. USA* **93(7)**, 2926-9.

[7] Tomishige, M., Sako, Y., Kusumi, A. (1998) Regulation mechanism of the lateral diffusion of band 3 in erythrocyte membranes by the membrane skeleton. *The Journal of Cell Biology* **142(4)**, 989-1000.

[8] Harms, G. S., Cognet, L., Lommerse, P. H., Blab, G. A., Schmidt, T. (2001). Autofluorescent proteins in single-molecule research: Applications to live cell imaging microscopy. *Proc. Nat. Acad. Sci.* **80**, 2396 - 2408.

[9] Koopmans, W. J. A., Buning, R., Schmidt, T., van Noort, J. (2009) spFRET using alternating laser excitation and FCS reveals progressive DNA unwrapping in nucleosomes. *Biophys. J.* **97(1)**, 195-204.

[10] Martin, D. S., Forstner, M. B., Käs, J. A. (2002) Apparent subdiffusion inherent to single particle tracking. *Biophys. J.* **83(4)**, 2109-2117.

[11] McHale, K., Berglund, A.J., Mabuchi, H.(2007) Quantum dot photon statistics measured by three-dimensional particle tracking. *Nano Letters* **7(11)**,3535-3539.

[12] Cang, H., Xu, C.S., Yang, H. (2008) Progress in single-molecule tracking spectroscopy. *Chemical Physics Letters* **457 (4-6)** 285 - 291.

[13] Sahl, S.J., Leutenegger, M., Hilbert, M., Hell, S.W., Eggeling, C.(2010) Fast molecular tracking maps nanoscale dynamics of plasma membrane lipids. *Proc Natl Acad Sci USA* **107(15)** 6829- 6834.

[14] Goulian, M., Simon, S. M.. (2000) Tracking single proteins within cells. *Biophys. J.* **79(4)**, 2188-98.

[15] Semrau, S., Schmidt, T. (2007) Particle image correlation spectroscopy (PICS): Retrieving nanometer-scale correlations from high-density single-molecule position data. *Biophys. J.* **92(2)**, 613-621.